PNAS RESEARCH ARTICLE | CHEMISTRY PHYSICS

Generating interstitial water within the persisting tetrahedral H-bond network explains density increase upon compressing liquid water

Mirko Förster[a,1], Nnanna Ukoji[b,1], Christoph J. Sahle[c,2], Johannes Niskanen[d], Robin Sakrowski[a], Göran Surmeier[a], Christopher Weis[a], Tetsuo Irifune[e], Sho Imoto[f], Hasan Yavas[g,h], Simo Huotari[i], Dominik Marx[f], Christian Sternemann[a], and John S. Tse[b,2]

Affiliations are included on p. 8.

Edited by Pablo Debenedetti, Princeton University, Princeton, NJ; received February 23, 2024; accepted July 16, 2024

Despite its ubiquitous nature, the atomic structure of water in its liquid state is still controversially debated. We use a combination of X-ray Raman scattering spectroscopy in conjunction with ab initio and path integral molecular dynamics simulations to study the local atomic and electronic structure of water under high pressure conditions. Systematically increasing fingerprints of non-hydrogen-bonded H_2O molecules in the first hydration shell are identified in the experimental and computational oxygen K-edge excitation spectra. This provides evidence for a compaction mechanism in terms of a continuous collapse of the second hydration shell with increasing pressure via generation of interstitial water within locally tetrahedral hydrogen-bonding environments.

structure of water | high-density form of water | X-ray Raman scattering

Significance

Water is one of the most ubiquitous substances known, yet its many thermodynamic and structural anomalies defy a general understanding at the atomic scale. Change of pressure, one of the canonical thermodynamic variables, is able to drive the system to new equilibria with different properties notably including structure. Here, we study the oxygen K-edge spectrum of strongly compressed water at ambient temperature and identify a continuously increasing spectral feature as a fingerprint of interstitial water molecules that are squeezed into the persisting fluctuating tetrahedral hydrogen-bonded network—providing the microscopic mechanism that allows the enormous density increase of compressed water.

Although water has been studied extensively for many years, the basic structural and dynamical properties of this elusive liquid are still not well understood (1–3). In the near-ambient solid phases of water, such as ice I_h, each water molecule is tetrahedrally hydrogen-bonded (H-bonded) to four neighboring water molecules. In the liquid state, this H-bond network is assumed to not be destroyed but to fluctuate on a pico- to nanosecond time scale due to disruptions caused by thermal fluctuations (4–7). One of the primary questions about the structure of liquid water at the microscopic level persists: Can it be described by a homogeneous and continuous distribution of H_2O moities (8–11) or is there a need to invoke the coexistence of two distinct forms of the liquid (12–14)? Connections have been made between the theory of the ambient liquid and regions of deeply supercooled water where the two structurally distinct forms of water have been proposed to exist (12, 15–17). Similar ideas remain controversial for supercritical water, namely its description in terms of low-density gas-like versus high-density liquid-like forms including debates on Widom, Frenkel, or Fisher–Widom lines (18–24).

In analogy to the low- and high-density amorphous ice phases (25–27), the proposed low-density form of water is assumed to have a close-to-tetrahedral local structure while the proposed high-density form possesses an asymmetric local H-bond coordination and a distorted first hydration shell with a "fifth" molecule intruding into the first coordination shell. Although the coexistence of these two structural species can explain some anomalous properties of water and the fact that recent experimental (28–30) and theoretical (31, 32) evidence supports this conjecture in the supercooled state of water, the true structure of liquid water is still debated.

Extrapolation of partial neutron structure factors measured at different pressures has been used to determine the spatial density function of the two putative extreme forms of water (33). In that study, the transformation from the low-density to high-density form of water is associated with a breaking of H-bonds between the first and second coordination shells and was therefore referred to as the collapse of the latter. Recent ultrafast X-ray structure factor measurements of the supercooled liquid obtained by evaporatively cooling of liquid droplets (28) and isochoric heating of high-density amorphous ice seem to be congruent with a liquid–liquid transition in the deep supercooled regime at pressures of several kbar (34).

Apart from the fundamental interest in the anomalous behavior, pressure-induced changes of the molecular structure of liquid water are relevant to a variety of research fields (35–40). The pressure evolution of the structure of liquid water is especially interesting for a deeper understanding of the survival mechanism of marine animals living at great depth (41–43). At corresponding hydrostatic compression, a nonmonotonous

Author contributions: C.J.S., C.S., and J.S.T. designed research; M.F., N.U., C.J.S., J.N., R.S., G.S., C.W., S.I., H.Y., S.H., D.M., C.S., and J.S.T. performed research; C.J.S. and T.I. contributed new reagents/analytic tools; M.F., N.U., C.J.S., J.N., C.W., S.H., and C.S. analyzed data; and M.F., N.U., C.J.S., J.N., D.M., C.S., and J.S.T. wrote the paper.

The authors declare no competing interest.

This article is a PNAS Direct Submission.

Copyright © 2024 the Author(s). Published by PNAS. This article is distributed under Creative Commons Attribution-NonCommercial-NoDerivatives License 4.0 (CC BY-NC-ND).

[1] M.F. and N.U. contributed equally to this work.

[2] To whom correspondence may be addressed. Email: sahle@esrf.fr or john.tse@usask.ca.

This article contains supporting information online at https://www.pnas.org/lookup/suppl/doi:10.1073/pnas.2403662121/-/DCSupplemental.

Published September 16, 2024.

Downloaded from https://www.pnas.org by 131.169.95.158 on April 8, 2025 from IP address 131.169.95.158.

pressure evolution of the attractive part of the protein–protein interaction with a distinct minimum at 2 kbar has been discovered and was related to pressure-induced changes in the microscopic structure of liquid water (44).

The intricate link between the electronic and the atomic structure renders spectroscopic probes a crucial tool for the investigation of the structure of water (45). Because of the element specificity and the local nature of the core-hole, X-ray absorption spectroscopy (XAS) experiments have been immensely important for the study of the local structure and H-bond topology around the absorbing oxygen sites (19, 45–48).

Since the oxygen 1*s* resonance energy lies in the soft X-ray regime, conventional XAS is prohibitively difficult for samples contained in a high-pressure apparatus. X-ray Raman scattering (XRS) spectroscopy (49–52) provides a unique tool to study shallow absorption edges of samples under extreme conditions since it utilizes hard X-rays via nonresonant inelastic X-ray scattering and has therefore been used in the past to study the oxygen K-edge of water at extreme conditions (19, 53–55).

Here, we use XRS in combination with extensive molecular dynamics simulations followed by XRS spectrum calculations from first principles to gain a deeper understanding of the evolution of the microscopic structure of compressed water. We find the oxygen K-edge to continuously change with increasing pressure. We assign these changes to additional water molecules that are squeezed into the first hydration shell without formation of H-bonds to the excited central molecule. These interstitial water molecules populate the voids offered by the persisting tetrahedral H-bonded network of the fluctuating disordered liquid while maintaining their own H-bonds. This structural feature is similar to the two interpenetrating water sublattices, which themselves form two distinct tetrahedrally H-bonded networks without any H-bonding between them, that are typical for some high-pressure ice phases. Thus, the same compaction mechanism via interstitial local neighbors, necessary to allow the density of water to increase much beyond 1 g/cm^3, is at work in the extremely compressed liquid and the high-pressure ice phases.

1. Results

Fig. 1*A* shows oxygen K-edge spectra measured at $T = 21.0\,^{\circ}\mathrm{C}$ and pressures between 1.0 bar and 9.3 kbar. Differences with respect to the spectrum of the ambient pressure sample are shown in part (*B*). To further aid the interpretation of the experimental spectra, we compare our experimental results to spectrum simulations within the transition potential half-core-hole approximation as implemented in the ERKALE code (56) (details in *Materials and Methods*) based on atomic structures obtained from two complementary simulation approaches, namely ab initio molecular dynamics (AIMD) based on density functional theory and path-integral centroid molecular dynamics (PICMD) using a nonempirical water potential. Panels (*C*–*F*) in Fig. 1 show the corresponding results of spectrum simulations based on these different simulation approaches.

Three features are evident in all spectra and are usually referred to as pre-, main-, and postedge (gray shaded areas in Fig. 1). The

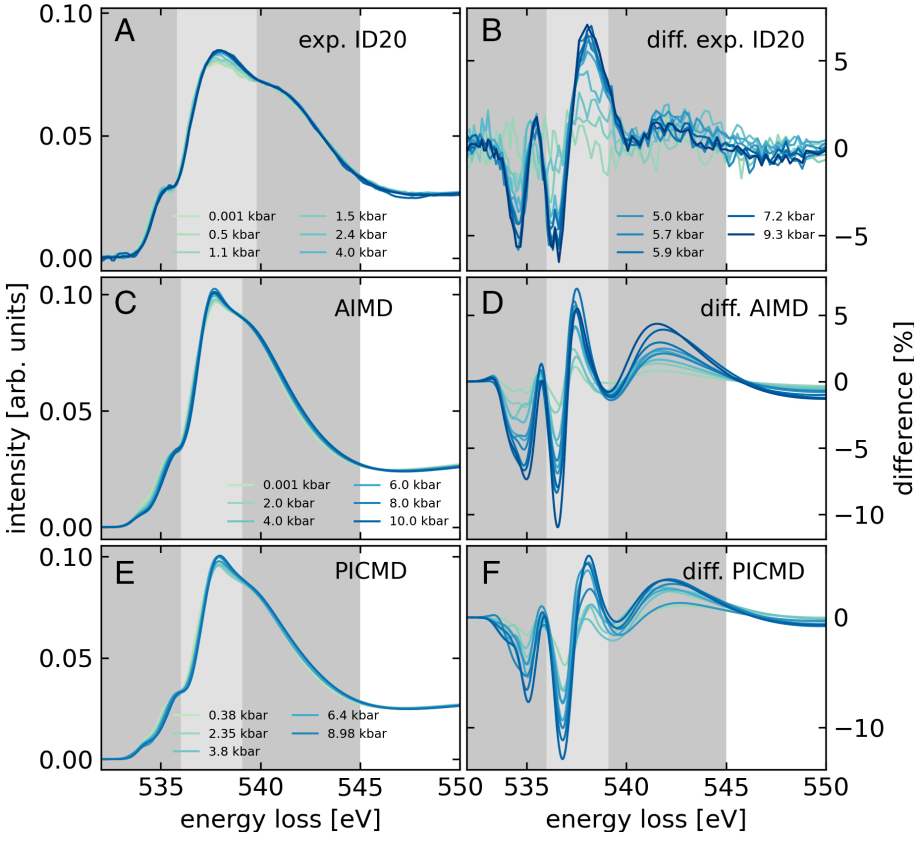

Fig. 1. Experimental XRS oxygen K-edge spectra at pressures between ambient and 9.3 kbar (*A*) and their differences with respect to the spectrum at ambient pressure (*B*) (legends shared between (*A* and *B*). (*C*–*F*) Spectra and spectral differences from simulations based on configurations sampled from AIMD and PICMD trajectories (legends shared between subfigures (*C*/*D*) and (*E*/*F*). The gray shaded areas indicate the three characteristic features of the oxygen K-edge of water: pre- (531.5 to 535.8 (536.0) eV), main- (535.8 (536.0) to 539.8 (539.1) eV), and postedge (539.8 (539.1) to 545.0 eV) for the experimental (theory) spectra. The averaged simulation spectra were shifted to meet the edge onset of the experimental data.

Downloaded from https://www.pnas.org by 131.169.95.158 on April 8, 2025 from IP address 131.169.95.158.

pre-edge region at 535 eV is described as a signature of distorted H-bonds and deviation from a tetrahedral structure. The spectral feature at the main edge region is suggested to reflect the approach of water molecules into the first hydration shell without formation of H-bonds to the excited water molecule, i.e., an increasing coordination number (55, 57), and to be sensitive to the H-bond distortions in liquid water (55). The postedge covers excitations into delocalized states and is sensitive to the arrangement of the first and second nearest-neighbor molecules and is, therefore, prominent in the tetrahedrally ordered low-density ices such as ice I_h. It has been shown that the postedge feature can be explained by shape-resonances due to excitations of the core electron to quasi-bound states with valence character (10, 53). The three spectral features have been shown to correlate with structural properties in the local vicinity of the excited oxygen site, however, these structural fingerprints must be viewed as averages of a fluctuating statistical ensemble, in which notable variation around the mean structural parameter—spectral feature relation exists (48).

Contrary to results reported much earlier (58), the pressure-induced changes of the oxygen K-edge are clearly observable in the present work, albeit small compared to the noise level of the previous study. Continuously increasing differences with respect to the ambient pressure spectrum are shown in Fig. 1*B*. Here, two minima at 534.5 eV and 536.0 eV are evidence of the blue shift of the spectra with increasing pressure and a broader maximum around 539 eV is indicative of the pressure-induced increase of spectral weight in the main-edge region.

The calculated XRS and difference spectra (Fig. 1 *C*–*F*) qualitatively reproduce the experimental findings: the intensity of the main-edge peak increases with pressure and no significant change in the pre-edge feature is observed. Correspondingly, the difference spectra show two minima in the region below 537 eV and a peak around 539 eV energy loss that becomes more pronounced with increasing pressure. However, differences exist between experiment and theory in the postedge region, where simulations predict increasing intensity with increasing pressure whereas the experimental spectra show almost constant spectral weight. We attribute this discrepancy to the known deficiencies of density functional theory–based methods to properly describe empty states and to the general difficulty of modeling low-energy continuum states. Recent GW-Bethe-Salpeter-Equation simulations of the oxygen K-edge of water demonstrate, albeit at great computational cost, that the experimental spectra can be reproduced quantitatively from first principles if self-consistent quasiparticle wave functions and a large Hilbert space, including unoccupied conduction orbitals, are used (59).

Apart from the slight blue shift, the shape of the pre-edge does not change notably as a function of pressure. Likewise, the postedge intensity remains almost constant throughout the entire pressure range and the strongest pressure-induced change is the intensity increase at the main-edge. Fig. 2*A* shows integrals of the difference spectra in the main-edge region as a function of pressure for the experimental (blue and red) and the simulated K-edge spectra (orange and green). The experimental difference spectra were integrated in a range from 537 eV to 540 eV, whereas a smaller range from 537.2 eV to 538.8 eV was chosen for the theoretical spectra due to the narrower features as discussed above. This follows the principle of correspondence, analyzing identifiable features that are reproduced by the simulations (60). The resulting main-edge intensity versus pressure curves were normalized to their area in between 1.0 bar and 5.0 kbar to account for slight differences between the different experimental runs and simulation results. Error bars are estimated based on

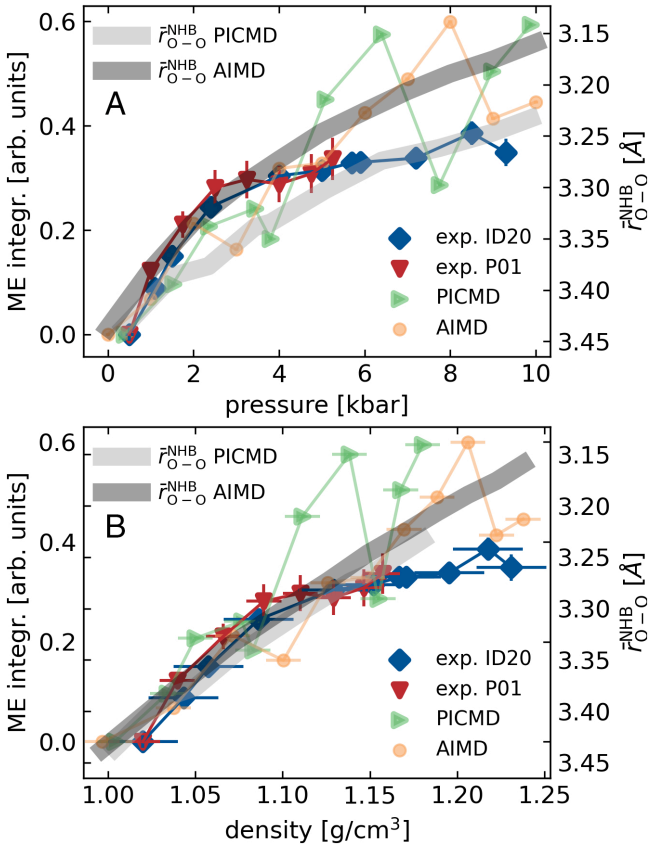

Fig. 2. (*A*) Integrated difference spectrum in the main-edge region (denoted ME integr.) as a function of pressure for the experimental and simulated oxygen K-edge spectra (see *Left* y-scale; different symbols label the two experiments and two simulations; see text). The broad dark (AIMD) and light (PICMD) gray lines represent the average (see *Right* y-scale; increasing from *Top* to *Bottom*) of the probability distribution functions of finding a fifth non-H-bonded water molecule depicted in Fig. 3 *C* and *D*. (*B*) Same as (*A*), but as a function of density as derived from the equation of state (61) to convert the experimental pressures. Corresponding data points are connected by straight lines to guide the eye.

slight variations of the integration ranges. After an initial steep increase up to 2.5 kbar, the rate of change for the integrated values decreases at higher pressures.

This trend is reproduced by both simulations and correlates as a function of increasing pressure with a decreasing average of the probability density for finding an interstitial fifth water molecule, as discussed below. The same main-edge intensity values are plotted as a function of density in part (*B*) of Fig. 2, where the experimental density was derived via the equation of state (61), showing similar behavior.

The overall satisfactory agreement of the salient spectral features between the two sets of calculated spectra and the experimental results as a function of pressure supports the validity of the two complementary methods, AIMD and PICMD. We thus use the underlying trajectories to extract utmost detailed information about the local structure around the scattering oxygen atoms of compressed water. The two sets of O-O radial distribution functions (RDFs) depicted in Fig. 3 *A* and *B* are found to be very similar as a function of pressure all the way from ambient up to 10 kbar. They feature the well-known nearest neighbor O-O peak at approximately 2.8 Å, which however shifts only slightly to smaller distances with increasing pressure. In stark contrast, the wider second maximum of the second shell around 4.5 Å broadens very significantly and gradually shifts toward the

Downloaded from https://www.pnas.org by 131.169.95.158 on April 8, 2025 from IP address 131.169.95.158.

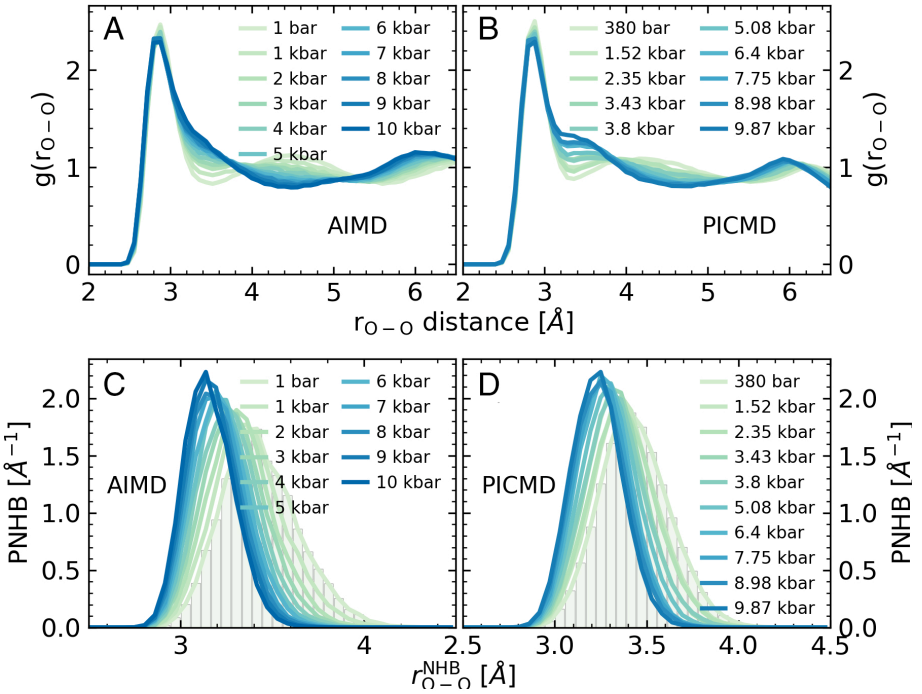

Fig. 3. Oxygen–oxygen radial distribution function of compressed water at 300 K calculated from (*A*) the AIMD and (*B*) the PICMD simulation trajectories. Probability distribution function for finding a fifth water molecule at distance r_{O-O}^{NHB} from a reference water molecule without forming an H-bond with the latter, as obtained from (*C*) AIMD and (*D*) PICMD simulations.

first coordination shell, thus creating a significantly enhanced probability at approximately 3.3 Å to find water molecules close to the reference molecule in the kbar regime compared to low pressures.

We computed the probability density of finding a fifth, interstitial, water molecule (PNHB) in the vicinity of each water molecule for the two simulation trajectories. PNHB is determined by counting the number of fifth-closest oxygen atoms in a given distance increment that are not H-bonded to the reference oxygen divided by the total number of fifth oxygen atoms (H-bonded or not; see *Materials and Methods* for details) (62, 63). The results are shown in Fig. 3 *C* and *D* for the AIMD and PICMD trajectories, respectively. These normalized probability distributions shift significantly to lower distances and sharpen considerably as a function of increasing pressure. Their average values $\bar{r}_{O-O}^{NHB}$ are indicative of how these additional water molecules approach the first shell with increasing pressure as reported by the broad gray lines in Fig. 2.

2. Discussion

2.1. Comparison to the Structure of Solid Water Phases. The sensitivity of the oxygen K-edge to the local structure and H-bond topology of the scattering or absorbing site has been demonstrated in many experimental and computational works (10, 19, 45, 48, 59, 64). Minute changes in the pre- and postedge manifest minute changes in the distributions of local tetrahedral arrangements of the H-bonded neighbors. As discussed above, spectral gain in the main-edge has been related to an increase of interstitial molecules that penetrate into the first coordination shell. These conclusions were drawn based on a comparison of experimental spectra of low and high-pressure ice phases (55, 65) as well as based on simulation work (48, 66).

The appearance of interstitial molecules in the first coordination shell is well known to appear when compressing the solid (27, 67, 68), but should be present even in the ambient liquid, since the O-O coordination number at ambient conditions exceeds four (19). Radial distribution functions from neutron and X-ray diffraction studies show clear evidence for the existence of additional molecules at short distances that do not H-bond to the reference water molecule when the liquid is compressed (33, 69–71).

The shared phase boundary between liquid water and various crystalline ice phases raises the question whether the local structural motifs of the high-density crystalline phases may be found in similar form in the liquid when comparing ice and liquid water at similar pressure. Ice I_h is an open and low-density structure, in which all water molecules experience the same local environment with interstitial voids large enough to host additional water molecules (72) and a second nearest neighbor distance of 4.5 Å. Half of these interstitial voids collapse when compressing ice I_h to form ice II (73) and the closest distance between oxygen atoms of two non-H-bonded H_2O molecules reduces to 3.24 Å. Likewise, in ice III and V the voids are partially collapsed. In these phases, H_2O molecules are arranged in a three-dimensional network of partially interconnected cages and/or rings with shortest next-nearest neighbor distances of 3.6 and 3.28 Å, respectively (74, 75). At even higher pressures, two fully separate yet interpenetrating H-bonded sublattices form, as is the case in ice VI and VII (and its proton-ordered counterpart ice VIII) (67, 68). In these fully self-clathrated structures, the closest non-H-bonded molecules are 2.86 Å and 3.35 Å apart, respectively.

We compare the recorded spectra of pressurized water with those of selected ice phases (I_h, III, and VI), all of which share a phase boundary with liquid water at lower temperature over large parts of the investigated pressure range. Fig. 4*A* shows

Downloaded from https://www.pnas.org by 131.169.95.158 on April 8, 2025 from IP address 131.169.95.158.

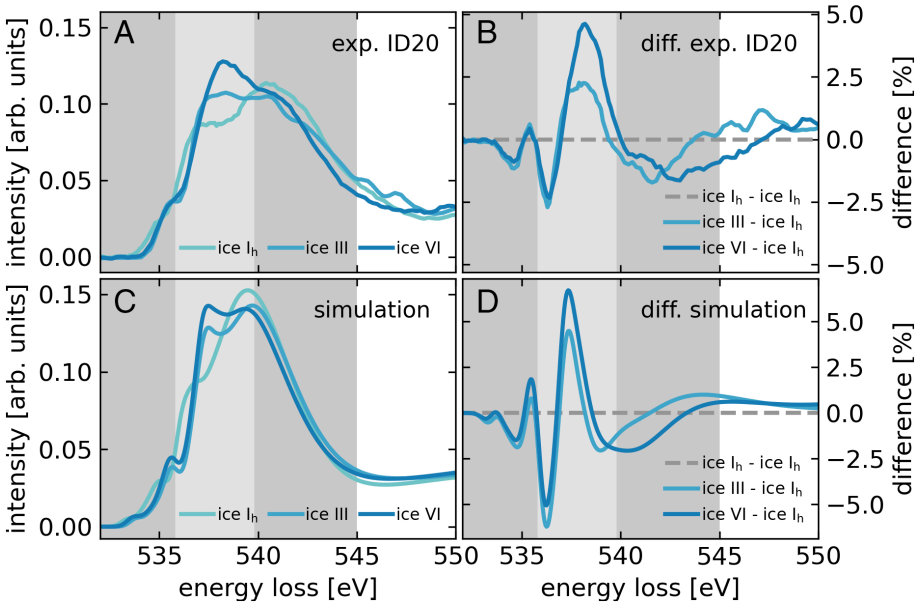

Fig. 4. (*A*) Experimental oxygen K-edge spectra of the ice phases I_h, III, and VI. (*B*) Experimental difference spectra of the ice phases III and VI with respect to the spectrum of hexagonal ice. (*C*) Simulated oxygen K-edge spectra (see text) of the ice phases I_h, III, and VI. (*D*) Difference spectra of the simulated ice III and VI spectra with respect to that of ice I_h. The spectra of ice I_h and VI are normalized as described in ref. 10. Due to the limited available energy loss range, the spectrum of ice III is only normalized to the available energy range, however, qualitative insight is still granted. Image Credit: Reprinted figure with permission from ref. 54. Copyright 2005 by the American Physical Society.

experimental oxygen K-edge spectra of ice I_h, ice III (spectrum digitized from ref. 54), and ice VI. Difference spectra between the high-pressure ice phases and ice I_h are shown in part (*B*). Corresponding simulation results based on transition potential approximation (TPA) calculations (56) of the well-known atomic structures are shown in parts (*C* and *D*). Even though the pre- and postedge features differ between the different ice phases, the most prominent relative spectral changes are observed in the main-edge region, as observed for the liquid. The difference spectra with respect to the spectrum of the lowest-density phase (ice I_h) show the characteristic shape also observed for the liquid phase with two minima around the pre-edge region and a maximum in the main-edge region (compare to Fig. 1). This indicates that the structural alterations water undergoes when subjected to increasing pressure may be similar to changes induced by the transitions from ice I_h to ice III and ice VI.

It should be noted, however, that this can only reflect the local structure surrounding the H_2O molecules, since liquid water, unlike ice I_h, III, and VI, exhibits no long-range order. This may explain the differences found at higher energy losses, as here the XRS spectrum is affected by scattering of free electrons in continuum states, the low-energy part of extended X-ray absorption fine structure. As mentioned earlier, the postedge does not change significantly as water is compressed, implying that the appearance of additional water molecules in the vicinity of the first shell does not significantly alter the potential barrier for a shape resonance. The barrier may predominantly be defined by the next-nearest neighbors in the absence of long-range order (10, 53, 76). Interpenetrating high-pressure water networks corresponding to, e.g., ice VI may consist of the local arrangements of two pentamers of water molecules, which structurally intertwine without forming H-bonds between each other. The results of a theoretical study investigating the interaction of rigid pentamers corroborate this hypothesis (77). We note that the water–ice I_h–ice III triple point is at 2 kbar (−22 °C), the same pressure that we see the initial steep increase of the main-edge intensity abate. The pressures probed here therefore coincide with pressures close to the stability field of (crystalline) structures with partially collapsed voids and onsets of interpenetration involving two H-bonded sublattices.

When ice I_h is subjected to pressure at low temperature, it transforms to high-density amorphous (HDA) ice at pressures close to the extrapolated melting curve of ice (78, 79). Even though temperatures are lower and pressures higher than here, the structural evolution may exhibit resemblances to the response of liquid water to pressure. Neutron diffraction data suggest that HDA ice, similar to ice VII yet without long-range order, is composed of interpenetrating but separate H-bond networks (27). Recent simulation work likewise showed that interstitial molecules in high pressure glassy water are not H-bonded to the reference molecule. However, the interstitial molecules form H-bonds of their own, rendering them topologically higher-order neighbors of the reference molecule (80). The comparison between the oxygen K-edge spectra of the solids and the compressed liquid at ambient temperatures suggests that locally, i.e., from the perspective of the excited oxygen reference atom, the compaction mechanisms are similar.

2.2. Comparison to Structural Models. The picture of how liquid water changes its H-bond structure as a function of compression into the kbar regime is not only confirmed by the two independent simulation approaches, AIMD and PICMD, but complemented with very detailed microscopic information on the local structure of high pressure water. In particular, over the entire pressure range studied here, the local water environment stays close to tetrahedrally coordinated akin to ambient water since the first peak in the O-O RDF as well as the peak in the distribution of the first to fourth oxygen neighbors are nearly unchanged (*SI Appendix*, Fig. S1). The probability of finding a second-nearest interstitial neighbor in the direct vicinity of the first shell significantly increases with pressure, as shown in Fig. 3 *C* and *D*, in line with previous simulation work (62, 81)

Downloaded from https://www.pnas.org by 131.169.95.158 on April 8, 2025 from IP address 131.169.95.158.

and experimental pair distribution analysis (33, 69–71). These interstitial water molecules are topological second to fourth H-bonded neighbors of the reference molecule (36, 80). Likewise, the oxygen orientation distribution, measuring angles between a reference oxygen atom and the various combinations of oxygen atoms of the first and second shell, clearly changes from a bimodal shape with maxima at 45° and 75° at ambient to a single maximum at approximately 65° at higher pressure (*SI Appendix*, Fig. S2). Again, this is attributed to an increasing amount of interstitial molecules that are created in the first hydration shell upon kbar compression.

Various experimental studies have confirmed the persistence of the H-bonds in the system with increasing pressure or likewise attribute the changes to the approach of additional water molecules to the first shell (38, 70, 82–85). For instance, in a femto-second mid-infrared pump–probe spectroscopy study of liquid water mixed with D_2O at a temperature of 25 °C and pressures up to 10 kbar, spectroscopic data were compared with molecular dynamics (MD) simulations (82). In the work, an increase of nonbonded molecules at short distances was observed without alterations to the local H-bonded tetrahedral configuration (82). The stability of the fourfold H-bonded structure of the immediate neighborhood is supported by X-ray diffraction measurements with a high q-range, where most of the changes in the pair distribution function were found to occur at higher distances, i.e., the interstitial neighboring molecules (84). Furthermore, THz spectroscopy combined with AIMD simulations (38, 85) also supports the existence of the tetrahedral H-bond network from ambient conditions up to about 10 kbar while being insensitive to non-H-bonded, interstitial water in that network (85). The unaffected shape of the pre-edge feature observed here as a function of pressure is direct evidence for the persistence of H-bonding in the compressed liquid. This suggests that the interstitial molecules, even though not H-bonded within the first shell of the excited molecule, are H-bonded to other molecules.

Having established the compression mechanism that triggers the continuous collapse of the second shell, we next investigate the nature of this transition by focusing on the associated rate of change as a function of compression. Fig. 2 *A* and *B* present a comparison of the integrated main-edge values from experiment to the average of PNHB, denoted $\bar{r}^{\mathrm{NHB}}_{\mathrm{O-O}}$, from both simulations approaches as a function of pressure and density, respectively. Despite some expected scatter of the main-edge integrals calculated from simulated spectra based on the AIMD or PICMD configurations, a continuous increase in the main-edge integral as a function of pressure and/or density is clearly observable. Very importantly, the increase of the main-edge spectral contribution is found to correlate with the continuously decreasing averages $\bar{r}^{\mathrm{NHB}}_{\mathrm{O-O}}$ of the PNHB distributions upon compression. This points to continuous pressure-induced structural changes that leave the tetrahedrally H-bonded neighbors relatively intact while non-H-bonded neighbors get pushed into the voids offered within the spanned tetrahedral network.

The measured oxygen K-edge spectra constitute averages over the individual spectra of the underlying atomistic local structures subject to the given temperature and pressure conditions (48). These local structures represent a continuous range of configurations that explore the thermodynamically accessible phase space. It has been shown that the main structure-spectral relationships established via comparison of spectra from ice I_h, liquid, and supercritical water may be recovered from a single simulation of liquid water at ambient conditions simply due to the variation of weights of local configurations within the statistical ensemble (48). In the current study of compressed water at room temperature, pressure drives the ensemble away from the ambient equilibrium, as characterized by open H-bonded tetrahedral nearest-neighbor environments, toward a situation where much of the open space, i.e., the voids between H-bonded water molecules, gets populated by additional water molecules, the interstitials, which are also close neighbors but not H-bonded.

3. Summary and Outlook

The characterization of the structure of liquid water poses a formidable challenge for experiment and theory. Conventional scattering techniques can provide information on the long to medium-range ordering. Semilocal probes, such as vibrational spectroscopy, are helpful in determining interactions between atoms. Here, we employed a site-specific technique, namely X-ray Raman scattering spectroscopy, to study the oxygen core level electronic excitation spectrum to reveal the effect of pressure on the microscopic structure of liquid water up to the multi-kbar regime. In concert with two complementary molecular dynamics simulations, ab initio and centroid path integral molecular dynamics, we finally disclose the underlying molecular picture at the level of the H-bonding network response to strong compression of liquid water.

No significant change in the oxygen K pre-edge feature was observed despite differences related to the blue shift of the edge. This indicates that there is no substantial alteration of the nearest neighbor H-bonds in contrast to, for example, observations for supercritical water (19, 86, 87). However, distinct changes of the main-edge region are revealed with a peculiar pressure dependence showing a continuous enhancement of the main-edge intensity. The excitations in this energy range of the main-edge have been shown to be sensitive to water molecules in the second coordination shell and the intermediate range order (59). The fact that only the main-edge evolves significantly as a function of pressure in contrast to the pre- and the postedge clearly indicates that the underlying structural alterations are driven by changes that are not accompanied by significant H-bond breaking, thus maintaining the local tetrahedral order even upon compression of liquid water up to 10 kbar.

The experimental XRS patterns and the difference spectra relative to ambient pressures were reproduced by spectra calculated based on both AIMD and PICMD molecular dynamics trajectories, indicating that these vastly different simulation approaches independently provide reliable representations of the liquid structure as a function of compression. Having validated the simulations by capturing the pressure-induced XRS main-edge changes, detailed analyses of the trajectories show that water molecules from the second coordination shell are squeezed into the interstitial voids available in the essentially unaltered tetrahedral H-bond network by the application of pressure without the formation of H-bonds with the water molecules in the first hydration shell.

Thus, we directly assign here the experimentally observed growing oxygen K main-edge intensity to the population of these voids with interstitial water molecules that are not H-bonded to the excited molecule. The persistent shape of the pre-edge with increasing pressure indicates that these interstitial water molecules form H-bonds of their own. This provides the compaction mechanism in pressurized water that allows for the enormous density increase of liquid water to 1.243 g/cm^3

Downloaded from https://www.pnas.org by 131.169.95.158 on April 8, 2025 from IP address 131.169.95.158.

at 10 kbar. Incidentally, the rate of change of that integrated main-edge intensity with pressure is close to the thermodynamic conditions of the transition regime from ice III via ice V to ice VI at lower temperature, a transition from a single H-bond network to two separate but interpenetrating such networks upon compression. In the latter case, H-bonded water molecules in one network are non-H-bonded to the second network and are, thus, interstitial waters therein. This comparison to structurally well-defined ice polymorphs provides additional credence to our view of a continuous formation of interstitial water molecules hosted in the voids of the essentially unperturbed tetrahedral H-bonded network in compressed liquid water at ambient temperature.

4. Materials and Methods

4.1. X-ray Raman Experiments. Preliminary XRS measurements on water under high pressure were performed at beamline P01 of PETRA III and beamline BLU12 at Spring-8. The experimental setup of both facilities has been documented elsewhere (88, 89). At P01, a spindle-driven hydrostatic pressure cell equipped with nano-polycrystalline diamond windows (90) and a pressure gauge for pressure estimation was used (91). The uncertainty in pressure is about 100 bar at the highest pressure using such hydrostatic pressure cell. At BLU12, a panoramic diamond anvil cell (DAC) was applied. Based on the experience gained with these experiments, final measurements were performed at beamline ID20 of the European Synchrotron Radiation Facility using a panoramic DAC equipped with 800 μm culet Boehler-Almax shaped diamonds (92). The sample was placed into a 400 μm hole in an X-ray transparent beryllium gasket together with a small ruby sphere for online pressure estimation via the pressure shift of the ruby luminescence (93), uncertainties in pressure are of the order of 250 bar.

At ID20, photons from four consecutive U26 undulators were monochromatized by a combination of a Si(111) high-heat-load monochromator and a Si(311) channel-cut postmonochromator. The beam was focused to 20 × 20 μm^2 at the sample position by a mirror system in Kirkpatrick-Baez geometry. We used the large-solid-angle spectrometer of ID20 employing 36 of 72 spherically bent Si(660) analyzer crystals due to the restricted opening angles of the DAC (94). The 36 analyzer crystals were placed in the vertical scattering plane (σ polarization) with 24 analyzer crystals in transmission geometry (momentum transfer $q = 2.4 \pm 0.4\,\text{Å}^{-1}$) and 12 analyzer crystals in backscattering geometry ($q = 9.0 \pm 0.4\,\text{Å}^{-1}$) (only low-$q$ data shown). To measure energy losses in the vicinity of the oxygen K-edge, the incident energy was scanned between 10.21 keV to 10.30 keV. The overall energy resolution was 0.7 eV.

At P01, the XRS spectra were measured using the XRS spectrometer equipped with 12 spherically bent Si(660) analyzer crystals 7 of which were used owing to the restricted field of view by the cell geometry. The incident energy was scanned with a Si(311) monochromator in a range from 10.2 keV to 10.235 keV with an overall energy resolution of approximately 0.8 eV using a beam size of 150 × 150 μm^2. The spectrometer was set to an average scattering angle of 26° resulting in a momentum transfer of $q = 2.3 \pm 0.4\,\text{Å}^{-1}$.

All XRS data analysis was performed using the XRStools program package (50). The same program package was utilized for further data treatment, i.e., consistency checking of the individual spectra of each analyzer crystal and each scan before merging, background subtraction, and normalization of the final spectra. The spectra were normalized to the area between 522 eV and 595 eV (527 eV and 550 eV for P01 data). The dataset recorded at ID20 extends to the highest pressures and provides the best signal-to-noise ratio and is therefore presented primarily in the above discussion.

4.2. Water Structural Model from Molecular Dynamics Calculations. Two independent sets of structural ensembles of compressed water at 300 K as a function of pressure up to 10 kbar were obtained from two complementary advanced MD simulations. Ab initio (AIMD) simulations (95) were carried out with the QUICKSTEP module of the CP2k software package based on Born–Oppenheimer propagation (96). The RPBE density functional (97) together with the D3 dispersion correction (using the two-body terms and zero damping) (98) was used in combination with the triple-zeta TZV2P basis set (99, 100). A total of 128 water molecules was simulated within a periodic cubic box with constant volume and a box length between 14.572 Å and 15.662 Å depending on the pressure (from 1 bar up to 10 kbar) and thus density of the system at 300 K according to the accurate experimental equation of state (61). Massive Nosé-Hoover chain thermostats were set to 300 K to establish the canonical ensemble. This AIMD approach has been demonstrated (36) to perform well for liquid water at 300 K from 1 bar to 10 kbar.

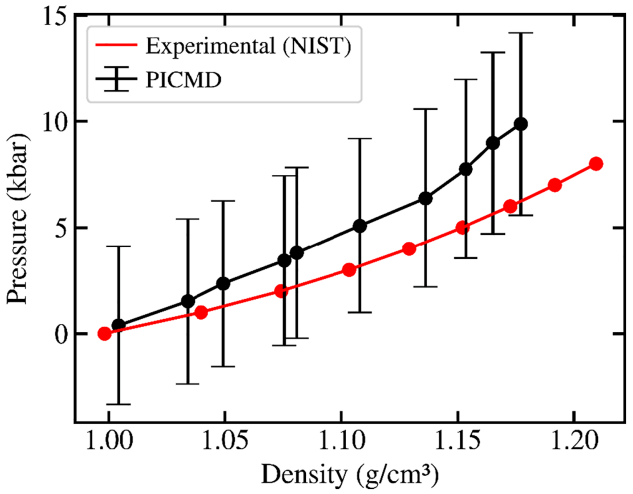

Fig. 5. Comparison of the experimental density (from ref. 61) to the computational equation of state based on the PICMD simulations; see text.

The second set of configurations depending on pressure was obtained from PICMD simulations (101) of 64 water molecules with interatomic potentials fitted to very accurate quantum chemistry calculations. The simulations were performed using an in-house, parallelized MD code that employed the flexible, all-atom polarizable Thole-type interaction potential (TTM2.1-F) (102, 103). Canonical (NVT) ensemble calculations on a 64-water system at 300 K were performed. PICMD replaces each quantum particle (hydrogen and oxygen) with a harmonic-beads ring-polymer and formulates the equation of motion with the centroid of the harmonic rings (104). In the present calculation, 16 beads were used to represent each quantum particle. The coupled equations of motion were solved with a time step of 0.01 fs. The total simulation time was 1 ns. The isotropic pressure at each density was the average of the principal components of the stress tensor obtained by appropriately adjusting the size of the simulation cell, which provides the computed equation of state shown in Fig. 5. The error bars associated with each pressure point were estimated from the time-averaged fluctuations of the principal components of the stress tensor after thermodynamic equilibration. The agreement is fair but certainly better than previous calculations even though the densities were underestimated with increasing pressure. The discrepancy is most likely due to the fact that the TTM2-F potential was parameterized for water at ambient pressure. The density obtained at zero pressure and 300 K was 1.003 g/cm^3 in good agreement with the experimental value. Furthermore, as reported earlier, the freezing point of ambient water is also well reproduced by our PICMD calculations (105).

4.3. Theoretical Modeling of XRS Spectra: Cluster Model Approach. Oxygen K-edge Spectra within the TPA were calculated based on atomic clusters cut from the trajectories of both, the AIMD and the PICMD, simulation trajectories using the ERKALE program package (56). Two different basis sets were used for the calculations. We used Dunning's standard augmented correlation consistent polarized valence double zeta basis set for all atoms in the system except for the excited oxygen atom, for which we used the IGLO-III basis set (106). In addition, once the convergence of the self-consistent field was reached, the basis set of the excited oxygen atom was extended with diffuse functions to further refine the description of the virtual orbitals. The energy loss scale of each individual

Downloaded from https://www.pnas.org by 131.169.95.158 on April 8, 2025 from IP address 131.169.95.158.

oxygen K-edge spectrum was set by calculating the difference in the total energy of the first core-excited state and the ground state for each individual cluster. For each spectrum at given pressure, approximately 750 spectra were calculated based on clusters centered around different oxygen sites of the simulation trajectories, which were then averaged to obtain a well-converged structural average spectrum. All simulations were performed at a momentum transfer value of $q = 2.65$ Å^{-1}, close to the experimental value. After averaging all spectra at a certain pressure, a Gaussian broadening scheme with a linearly increasing full width at half maximum from 0.6 eV to 8 eV between 536 eV and 545 eV was applied. This scheme was used to account for finite lifetime effects and the experimental broadening of the apparatus (107). The final average spectra were shifted on the energy loss scale to coincide with their experimental counterpart.

4.4. Structural Analysis.

4.4.1. Hydrogen bonds. Hydrogen bonds were evaluated subject to geometric criteria (48, 108), i.e., two water molecules are H-bonded if the two oxygen atoms are separated by less than 3.5 Å and the hydrogen-donor-acceptor angle is less than or equal to 30°.

4.4.2. PNHB. The probability distribution for finding a fifth water molecule at distance r_{O-O}^{NHB} from a reference water molecule without formation of an H-bond with this reference molecule is calculated following ref. 109. For each water molecule *i*, the neighboring molecules are ordered according to their radial distance of their oxygen atoms. The probability of finding a water molecule not H-bonded to *i* at a given distance r_{O-O}^{NHB} is then calculated by the number of water molecules not H-bonded to *i* divided by the total number of water molecules found at r_{O-O}^{NHB}.

Data, Materials, and Software Availability. Ascii data have been deposited in zenodo (TBD). Previously published data were used for this work (54).

ACKNOWLEDGMENTS. We acknowledge the European Synchrotron Radiation Facility for provision of synchrotron radiation facilities for proposal IH-SC-1598 and we would like to thank F. Gerbon for assistance and support in using beamline ID20. We acknowledge Deutsches Elektronen-Synchrotron (DESY) (Hamburg, Germany), a member of the Helmholtz Association HGF, for the provision of experimental facilities. Parts of this research were carried out at PETRA III. Beamtime at beamline P01 was allocated for proposal I-20170393. We acknowledge the Taiwan beamline BL12XU of Spring8 for initial test studies. We thank M. Paulus, F. Lehmkühler and M. Tolan for fruitful discussions. Funded by the Deutsche Forschungsgemeinschaft (German Research Foundation) under Germany's Excellence Strategy–EXC 2033–390677874–RESOLV. The The ab initio molecular dynamics simulations were carried out using SuperMUC/NG at LRZ München as well as HPC–RESOLV, HPC@ZEMOS and BOVILAB@RUB. J.S.T and N.U. wish to thank Dr. X. Yong for assistance with the path integral centroid molecular dynamics simulations. The Natural Sciences and Engineering Research Council of Canada is acknowledged for support via a DISCOVERY grant.

Author affiliations: [a]Fakultät Physik/DELTA, Technische Universität Dortmund, Dortmund 44227, Germany; [b]Department of Physics and Engineering Physics, University of Saskatchewan, Saskatoon, SK S7N 5E2, Canada; [c]ESRF, The European Synchrotron, Grenoble Cedex 9 38043, France; [d]Department of Physics and Astronomy, University of Turku, Turun yliopisto FI-20014, Finland; [e]Geodynamics Research Center, Ehime University, Matsuyama 790, Japan; [f]Lehrstuhl für Theoretische Chemie, Ruhr-Universität Bochum, Bochum 44780, Germany; [g]Deutsches Elektronen-Synchrotron, Hamburg 22607, Germany; [h]Linac Coherent Light Source, SLAC National Accelerator Laboratory, Menlo Park, CA 94025; and [i]Department of Physics, University of Helsinki, Helsinki FI-00014, Finland

1. P. Ball, Water is an active matrix of life for cell and molecular biology. *Proc. Natl. Acad. Sci. U.S.A.* **114**, 13327–13335 (2017).
2. E. Brini *et al*., How water's properties are encoded in its molecular structure and energies. *Chem. Rev.* **117**, 12385–12414 (2017).
3. J. R. Errington, P. G. Debenedetti, Relationship between structural order and the anomalies of liquid water. *Nature* **409**, 318–321 (2001).
4. F. H. Stillinger, Water revisited. *Science* **209**, 451–457 (1980).
5. I. Ohmine, H. Tanaka, Fluctuation, relaxations, and hydration in liquid water. Hydrogen-bond rearrangement dynamics. *Chem. Rev.* **93**, 2545–2566 (1993).
6. A. Luzar, D. Chandler, Hydrogen-bond kinetics in liquid water. *Nature* **379**, 55–57 (1996).
7. D. Laage, J. T. Hynes, A molecular jump mechanism of water reorientation. *Science* **311**, 832–835 (2006).
8. S. Sastry, P. G. Debenedetti, F. Sciortino, H. E. Stanley, Singularity-free interpretation of the thermodynamics of supercooled water. *Phys. Rev. E* **53**, 6144 (1996).
9. T. Head-Gordon, M. E. Johnson, Tetrahedral structure or chains for liquid water. *Proc. Natl. Acad. Sci. U.S.A.* **103**, 7973–7977 (2006).
10. J. Niskanen *et al*., Compatibility of quantitative X-ray spectroscopy with continuous distribution models of water at ambient conditions. *Proc. Natl. Acad. Sci. U.S.A.* **116**, 4058–4063 (2019).
11. A. Soper, Is water one liquid or two? *J. Chem. Phys.* **150**, 234503 (2019).
12. O. Mishima, H. E. Stanley, The relationship between liquid, supercooled and glassy water. *Nature* **396**, 329–335 (1998).
13. P. Wernet *et al*., The structure of the first coordination shell in liquid water. *Science* **304**, 995–999 (2004).
14. C. Huang *et al*., The inhomogeneous structure of water at ambient conditions. *Proc. Natl. Acad. Sci. U.S.A.* **106**, 15214–15218 (2009).
15. P. H. Poole, F. Sciortino, U. Essmann, H. E. Stanley, Phase behaviour of metastable water. *Nature* **360**, 324–328 (1992).
16. P. G. Debenedetti, Supercooled and glassy water. *J. Phys. Condens. Matter* **15**, R1669–R1726 (2003).
17. P. Gallo *et al*., Water: A tale of two liquids. *Chem. Rev.* **116**, 7463–7500 (2016).
18. L. Xu *et al*., Relation between the widom line and the dynamic crossover in systems with a liquid-liquid phase transition. *Proc. Natl. Acad. Sci. U.S.A.* **102**, 16558–16562 (2005).
19. C. J. Sahle *et al*., Microscopic structure of water at elevated pressures and temperatures. *Proc. Natl. Acad. Sci. U.S.A.* **110**, 6301–6306 (2013).
20. G. Galli, D. Pan, A closer look at supercritical water. *Proc. Natl. Acad. Sci. U.S.A.* **110**, 6250–6251 (2013).
21. P. Gallo, D. Corradini, M. Rovere, Widom line and dynamical crossovers as routes to understand supercritical water. *Nat. Commun.* **5**, 5806 (2014).
22. V. P. Sokhan, A. Jones, F. Cipcigan, J. Crain, G. J. Martyna, Molecular-scale remnants of the liquid-gas transition in supercritical polar fluids. *Phys. Rev. Lett.* **115**, 117801 (2015).
23. P. Sun, J. B. Hastings, D. Ishikawa, A. Q. R. Baron, G. Monaco, Two-component dynamics and the liquidlike to gaslike crossover in supercritical water. *Phys. Rev. Lett.* **125**, 256001 (2020).
24. F. Simeski, M. Ihme, Supercritical fluids behave as complex networks. *Nat. Commun.* **14**, 1996 (2023).
25. S. T. John, M. L. Klein, Pressure-induced phase transformations in ice. *Phys. Rev. Lett.* **58**, 1672 (1987).
26. J. Finney *et al*., Structure of a new dense amorphous ice. *Phys. Rev. Lett.* **89**, 205503 (2002).
27. S. Klotz *et al*., Structure of high-density amorphous ice under pressure. *Phys. Rev. Lett.* **89**, 285502 (2002).
28. J. A. Sellberg *et al*., Ultrafast X-ray probing of water structure below the homogeneous ice nucleation temperature. *Nature* **510**, 381–384 (2014).
29. L. Kringle, W. A. Thornley, B. D. Kay, G. A. Kimmel, Reversible structural transformations in supercooled liquid water from 135 to 245 K. *Science* **369**, 1490–1492 (2020).
30. K. Amann-Winkel *et al*., Liquid-liquid phase separation in supercooled water from ultrafast heating of low-density amorphous ice. *Nat. Commun.* **14**, 442 (2023).
31. P. G. Debenedetti, F. Sciortino, G. H. Zerze, Second critical point in two realistic models of water. *Science* **369**, 289–292 (2020).
32. T. E. Gartner III, P. M. Piaggi, R. Car, A. Z. Panagiotopoulos, P. G. Debenedetti, Liquid-liquid transition in water from first principles. *Phys. Rev. Lett.* **129**, 255702 (2022).
33. A. K. Soper, M. A. Ricci, Structures of high-density and low-density water. *Phys. Rev. Lett.* **84**, 2881 (2000).
34. K. H. Kim *et al*., Experimental observation of the liquid-liquid transition in bulk supercooled water under pressure. *Science* **370**, 978–982 (2020).
35. A. Okhulkov, Y. N. Demianets, Y. E. Gorbaty, X-ray scattering in liquid water at pressures of up to 7.7 kbar: Test of a fluctuation model. *J. Chem. Phys.* **100**, 1578–1588 (1994).
36. S. Imoto, H. Forbert, D. Marx, Water structure and solvation of osmolytes at high hydrostatic pressure: Pure water and tmao solutions at 10 kbar versus 1 bar. *Phys. Chem. Chem. Phys.* **17**, 24224–24237 (2015).
37. C. Schmidt, C. Manning, Pressure-induced ion pairing in $MgSO_4$ solutions: Implications for the oceans of icy worlds. *Geochem. Perspect. Lett.* **3**, 66–74 (2017).
38. H. Vondracek *et al*., Hydrogen-bonding in liquid water at multikilobar pressures. *J. Phys. Chem. B* **123**, 7748–7753 (2019).
39. T. Yamaguchi, N. Fukuyama, K. Yoshida, Y. Katayama, Ion solvation and water structure in an aqueous sodium chloride solution in the gigapascal pressure range. *J. Phys. Chem. Lett.* **12**, 250–256 (2020).
40. S. Imoto, D. Marx, How can protons migrate in extremely compressed liquid water? *Phys. Rev. Lett.* **125**, 086001 (2020).
41. P. H. Yancey, Organic osmolytes as compatible, metabolic and counteracting cytoprotectants in high osmolarity and other stresses. *J. Exp. Biol.* **208**, 2819–2830 (2005).
42. S. Imoto *et al*., Toward extreme biophysics: Deciphering the infrared response of biomolecular solutions at high pressures. *Angew. Chem. Int. Ed. Engl.* **55**, 9534–9538 (2016).
43. T. Ohto *et al*., Trimethylamine-n-oxide: Its hydration structure, surface activity, and biological function, viewed by vibrational spectroscopy and molecular dynamics simulations. *Phys. Chem. Chem. Phys.* **19**, 6909–6920 (2017).
44. M. A. Schroer *et al*., Nonlinear pressure dependence of the interaction potential of dense protein solutions. *Phys. Rev. Lett.* **106**, 178102 (2011).
45. T. Fransson *et al*., X-ray and electron spectroscopy of water. *Chem. Rev.* **116**, 7551–7569 (2016).
46. U. Bergmann *et al*., X-ray raman spectroscopy at the oxygen k edge of water and ice: Implications on local structure models. *Phys. Rev. B* **66**, 092107 (2002).

Downloaded from https://www.pnas.org by 131.169.95.158 on April 8, 2025 from IP address 131.169.95.158.

47. T. Pylkkanen *et al*., Temperature dependence of the near-edge spectrum of water. *J. Phys. Chem. B* **115**, 14544–14550 (2011).
48. J. Niskanen *et al*., Disentangling structural information from core-level excitation spectra. *Phys. Rev. E* **96**, 013319 (2017).
49. W. Schülke, *Electron Dynamics by Inelastic X-ray Scattering* (OUP Oxford, 2007), vol. 7.
50. C. J. Sahle *et al*., Planning, performing and analyzing X-ray Raman scattering experiments. *J. Synchrotron Rad.* **22**, 400–409 (2015).
51. C. Sternemann, M. Wilke, Spectroscopy of low and intermediate Z elements at extreme conditions: In situ studies of Earth materials at pressure and temperature via X-ray Raman scattering. *High Press. Res.* **36**, 275–292 (2016).
52. E. Alp, J. S. Tse, *Application of Inelastic Scattering of X-rays at High Pressure in High-pressure Molecular Spectroscopy* (Walter de Gruyter GmbH, 2022).
53. J. Tse, K. Tan, J. Chen, Oxygen k-edge xanes of crystalline and amorphous ice. *Chem. Phys. Lett.* **174**, 603–608 (1990).
54. Y. Cai *et al*., Ordering of hydrogen bonds in high-pressure low-temperature H_2O. *Phys. Rev. Lett.* **94**, 025502 (2005).
55. T. Pylkkanen *et al*., Role of non-hydrogen-bonded molecules in the oxygen K-edge spectrum of ice. *J. Phys. Chem. B* **114**, 3804–3808 (2010).
56. J. Lehtola, M. Hakala, A. Sakko, K. Hämäläinen, ERKALE-A flexible program package for X-ray properties of atoms and molecules. *J. Comput. Chem.* **33**, 1572–1585 (2012).
57. J. S. Tse, Mechanical instability in ice Ih. A mechanism for pressure-induced amorphization. *J. Chem. Phys.* **96**, 5482–5487 (1992).
58. H. Fukui, S. Huotari, D. Andrault, T. Kawamoto, Oxygen K-edge fine structures of water by X-ray Raman scattering spectroscopy under pressure conditions. *J. Chem. Phys.* **127**, 134502 (2007).
59. F. Tang *et al*., Many-body effects in the X-ray absorption spectra of liquid water. *Proc. Natl. Acad. Sci. U.S.A.* **119**, e2201258119 (2022).
60. J. Niskanen, A. Vladyka, J. A. Kettunen, C. J. Sahle, Machine learning in interpretation of electronic core-level spectra. *J. Electron Spectrosc. Relat. Phenom.* **260**, 147243 (2022).
61. W. Wagner, A. Pruß, The IAPWS formulation 1995 for the thermodynamic properties of ordinary water substance for general and scientific use. *J. Phys. Chem. Ref. Data.* **31**, 387–535 (2002).
62. A. M. Saitta, F. Datchi, Structure and phase diagram of high-density water: The role of interstitial molecules. *Phys. Rev. E* **67**, 020201 (2003).
63. X. Yong, J. S. Tse, N. J. English, optPBE-vdW density functional theory study of liquid water and pressure-induced structural evolution in ice ih. *Can. J. Chem.* **95**, 1205–1211 (2017).
64. A. Nilsson, L. G. Pettersson, Perspective on the structure of liquid water. *Chem. Phys.* **389**, 1–34 (2011).
65. J. S. Tse *et al*., X-ray raman spectroscopic study of water in the condensed phases. *Phys. Rev. Lett.* **100**, 095502 (2008).
66. W. Chen, X. Wu, R. Car, X-ray absorption signatures of the molecular environment in water and ice. *Phys. Rev. Lett.* **105**, 017802 (2010).
67. B. Kamb, Structure of ice VI. *Science* **150**, 205–209 (1965).
68. W. Kuhs *et al*., Structure and hydrogen ordering in ices VI, VII, and VIII by neutron powder diffraction. *Acta Crystallogr. A* **40**, C114–C115 (1984).
69. A. Wu, E. Whalley, G. Dolling, Neutron diffraction of heavy water to 15.6 kbar. *Mol. Phys.* **47**, 603–628 (1982).
70. T. Strässle *et al*., Structure of dense liquid water by neutron scattering to 6.5 GPa and 670 K. *Phys. Rev. Lett.* **96**, 067801 (2006).
71. G. Weck *et al*., Phase diagrams and isotopic effects of normal and deuterated water studied via X-ray diffraction up to 4.5 GPa and 500 K. *Phys. Rev. B* **80**, 180202 (2009).
72. A. Soper, The radial distribution functions of water and ice from 220 to 673 K and at pressures up to 400 MPa. *Chem. Phys.* **258**, 121–137 (2000).
73. B. Kamb, Ice II: A proton-ordered form of ice. *Acta Crystallogr.* **17**, 1437–1449 (1964).
74. B. Kamb, A. Prakash, C. Knobler, Structure of ice V. *Acta Crystallogr.* **22**, 706–715 (1967).
75. B. Kamb, A. Prakash, Structure of ice III. *Acta Crystallogr. A* **24**, 1317–1327 (1968).
76. J. S. Tse, Resonant enhancement in the valence orbital photoionization cross sections of xenon difluoride. *J. Chem. Phys.* **89**, 920–928 (1988).
77. M. Canpolat *et al*., Local structural heterogeneities in liquid water under pressure. *Chem. Phys. Lett.* **294**, 9–12 (1998).
78. O. Mishima, L. Calvert, E. Whalley, "Melting ice" I at 77 K and 10 kbar: A new method of making amorphous solids. *Nature* **310**, 393–395 (1984).
79. J. Tse *et al*., The mechanisms for pressure-induced amorphization of ice Ih. *Nature* **400**, 647–649 (1999).
80. R. Foffi, F. Sciortino, Structure of high-pressure supercooled and glassy water. *Phys. Rev. Lett.* **127**, 175502 (2021).
81. E. Schwegler, G. Galli, F. Gygi, Water under pressure. *Phys. Rev. Lett.* **84**, 2429 (2000).
82. S. Fanetti *et al*., Structure and dynamics of low-density and high-density liquid water at high pressure. *J. Phys. Chem. Lett.* **5**, 235–240 (2014).
83. Y. Katayama *et al*., Structure of liquid water under high pressure up to 17 GPa. *Phys. Rev. B* **81**, 014109 (2010).
84. L. B. Skinner *et al*., The structure of liquid water up to 360 MPa from X-ray diffraction measurements using a high Q-range and from molecular simulation. *J. Chem. Phys.* **144**, 134504 (2016).
85. S. Imoto, D. Marx, Pressure response of the THz spectrum of bulk liquid water revealed by intermolecular instantaneous normal mode analysis. *J. Chem. Phys.* **150**, 084502 (2019).
86. C. J. Sahle *et al*., Cation hydration in supercritical NaOH and HCl aqueous solutions. *J. Phys. Chem. B* **121**, 11383–11389 (2017).
87. M. Elbers *et al*., Ion association in hydrothermal aqueous NaCl solutions: Implications for the microscopic structure of supercritical water. *Phys. Chem. Chem. Phys.* **23**, 14845–14856 (2021).
88. D. Ketenoglu *et al*., X-ray raman spectroscopy of lithium-ion battery electrolyte solutions in a flow cell. *J. Synchrotron Rad.* **25**, 537–542 (2018).
89. Y. Cai *et al*., Optical design and performance of the taiwan inelastic X-ray scattering beamline (BL12XU) at SPring-8. *AIP Conf. Proc. (Am. Inst. Phys.)* **705**, 340–343 (2004).
90. T. Irifune, A. Kurio, S. Sakamoto, T. Inoue, H. Sumiya, Ultrahard polycrystalline diamond from graphite. *Nature* **421**, 599–600 (2003).
91. C. Krywka *et al*., Effect of osmolytes on pressure-induced unfolding of proteins: A high-pressure SAXS study. *Chem. Phys. Chem.* **9**, 2809–2815 (2008).
92. S. Petitgirard *et al*., A versatile diamond anvil cell for X-ray inelastic, diffraction and imaging studies at synchrotron facilities. *Rev. Sci. Instrum.* **90**, 095107 (2019).
93. G. Shen *et al*., Toward an international practical pressure scale: A proposal for an IPPS ruby gauge (IPPS-Ruby2020). *High Press. Res.* **40**, 299–314 (2020).
94. S. Huotari *et al*., A large-solid-angle X-ray Raman scattering spectrometer at ID20 of the European Synchrotron Radiation Facility. *J. Synchrotron Rad.* **24**, 521–530 (2017).
95. D. Marx, J. Hutter, *Ab Initio Molecular Dynamics: Theory and Implementation* (Cambridge University Press, Cambridge, 2009).
96. T. D. Kühne *et al*., CP2K: An electronic structure and molecular dynamics software package-Quickstep: Efficient and accurate electronic structure calculations. *J. Chem. Phys.* **152**, 194103 (2020).
97. B. Hammer, L. B. Hansen, J. K. Nørskov, Improved adsorption energetics within density-functional theory using revised Perdew-Burke-Ernzerhof functionals. *Phys. Rev. B* **59**, 7413 (1999).
98. S. Grimme, J. Antony, S. Ehrlich, H. Krieg, A consistent and accurate ab initio parametrization of density functional dispersion correction (DFT-D) for the 94 elements H-Pu. *J. Chem. Phys.* **132**, 154104 (2010).
99. S. Goedecker, M. Teter, J. Hutter, Separable dual-space Gaussian pseudopotentials. *Phys. Rev. B* **54**, 1703 (1996).
100. J. VandeVondele, J. Hutter, Gaussian basis sets for accurate calculations on molecular systems in gas and condensed phases. *J. Chem. Phys.* **127**, 114105 (2007).
101. J. Cao, G. A. Voth, A new perspective on quantum time correlation functions. *J. Chem. Phys.* **99**, 10070–10073 (1993).
102. C. J. Burnham, S. S. Xantheas, Development of transferable interaction models for water. IV. A flexible, all-atom polarizable potential (TTM2-F) based on geometry dependent charges derived from an ab initio monomer dipole moment surface. *J. Chem. Phys.* **116**, 5115–5124 (2002).
103. G. S. Fanourgakis, S. S. Xantheas, The flexible, polarizable, thole-type interaction potential for water (TTM2-F) revisited. *J. Phys. Chem. A* **110**, 4100–4106 (2006).
104. M. Tuckerman, *Ab Initio Molecular Dynamics and Ab Initio Path Integrals*, J. Grotendorst, D. Marx, A. Muramatsu, Eds. (John von Neumann Institute for Computing, 2002).
105. X. Yong, C. J. Burnham, N. J. English, J. S. Tse, Classical and path-integral molecular-dynamics study on liquid water and ice melting using non-empirical TTM2. 1-F model. *Mol. Phys.* **117**, 3241–3253 (2019).
106. U. Fleischer *et al*., "The IGLO-method: Ab-initio calculation and interpretation of NMR chemical shifts and magnetic susceptibilities" in *Deuterium and Shift Calculation*, P. Diehl, E. Fluck, H. Guenther, R. Kosfeld, J. Seelig, Eds. (Springer, 1991), pp. 165–262.
107. M. Cavalleri, M. Odelius, D. Nordlund, A. Nilsson, L. G. Pettersson, Half or full core hole in density functional theory X-ray absorption spectrum calculations of water? *Phys. Chem. Chem. Phys.* **7**, 2854–2858 (2005).
108. A. Luzar, D. Chandler, Effect of environment on hydrogen bond dynamics in liquid water. *Phys. Rev. Lett.* **76**, 928 (1996).
109. J. Russo, H. Tanaka, Understanding water's anomalies with locally favoured structures. *Nat. Commun.* **5**, 3556 (2014).

Downloaded from https://www.pnas.org by 131.169.95.158 on April 8, 2025 from IP address 131.169.95.158.